

The inflow signature toward different evolutionary phases of massive star formation

Mihwa Jin¹, Jeong-Eun Lee¹, Kee-Tae Kim², Neal J. Evans II³

¹ School of Space Research, Kyung Hee University, 1732, Deogyong-daero, Giheung-gu, Yongin-si, Gyeonggi-do, 17104, Korea; mihwajin.sf@gmail.com, jeongeun.lee@khu.ac.kr

² Korea Astronomy and Space Science Institute, 776 Daedeokdae-ro, Yuseong-gu, Daejeon 34055, Korea; ktkim@kasi.re.kr

³ Department of Astronomy, University of Texas at Austin, 1 University Station, C1400, Austin, Texas 78712-0259; nje@astro.as.utexas.edu

Received _____; accepted _____

ABSTRACT

We analyzed both HCN $J=1-0$ and HNC $J=1-0$ line profiles to study the inflow motions in different evolutionary stages of massive star formation: 54 infrared dark clouds (IRDCs), 69 high-mass protostellar object (HMPOs), and 54 ultra-compact HII regions (UCHIIs). The inflow asymmetry in HCN spectra seems to be prevalent throughout all the three evolutionary phases, with IRDCs showing the largest excess in blue profile. In the case of HNC spectra, the prevalence of blue sources does not appear, excepting for IRDCs. We suggest that this line is not appropriate to trace inflow motion in evolved stages of massive star formation because the abundance of HNC decreases at high temperatures. This result spotlights the importance of considering chemistry in the dynamics study of massive star-forming regions. The fact that the IRDCs show the highest blue excess in both transitions indicates that the most active inflow occurs in the early phase of star formation, i.e., the IRDC phase rather than in the later phases. However, mass is still inflowing onto some UCHIIs. We also found that the absorption dips of the HNC spectra in 6 out of 7 blue sources are red-shifted relative to their systemic velocities. These red-shifted absorption dips may indicate global collapse candidates, although mapping observations with better resolution are needed to examine this feature in more detail.

Subject headings:

1. Introduction

Massive stars are considered to be decisive players in the physical and chemical evolution of galaxies, injecting energetic feedbacks into their surroundings. In recent years, there have been many studies trying to examine the formation mechanism of high-mass stars, suggesting an evolutionary sequence of massive star formation as follows. First, the formation of massive stars begins in an infrared dark cloud (IRDC) identified as dark extinction features against the bright Galactic mid-infrared background (Egan et al. 1998; Simon et al. 2006a). Their cold ($\lesssim 25$ K) and dense ($\gtrsim 10^5$ cm $^{-3}$) properties and strong (sub)millimeter emissions (e.g., Rathborne et al. 2006) suggest the regions as ideal birthplaces of massive stars. The central condensation then begins heating its environment, evolving to become a high-mass protostellar object (HMPO). They are luminous infrared point-like sources ($L_{\text{bol}} \geq 10^3 L_{\odot}$) without associated radio continuum emission (Molinari et al. 1996, 2000; Sridharan et al. 2002; Beuther et al. 2002). This protostar continues to gain mass and evolves to produce UV photons, ionizing the gas, becoming an ultracompact HII region (UCHII). UCHIIs are very small ($D \lesssim 0.1$ pc), dense ($n_e \gtrsim 10^4$ cm $^{-3}$), and bright ($EM \gtrsim 10^7$ pc cm $^{-6}$) ionized regions (Wood & Churchwell 1989; Kurtz et al. 1994; Kim & Koo 2001). The objects are considered to represent the childhood of HII regions.

Nevertheless, the formation mechanism for the massive stars is still in debate. There are two competing theories describing the massive star formation: turbulent core accretion and competitive accretion (McKee & Ostriker 2007; Zinnecker & Yorke 2007; Bodenheimer 2011). In the turbulent core accretion model, high-mass cloud cores form from a much larger molecular cloud clump, which is supported by quasi-virialized turbulent flows. The material that ends up as stars can be essentially determined by the process of fragmentation of the cloud clump because the cores are almost non-interacting and the remainder of

the clump seldom affects the inflowing process (McKee & Tan 2003). This scenario well explains an initial mass function similar to a core mass function, which is consistent with observations (Motte et al. 1998; Beuther & Schilke 2004; Krumholz & Tan 2007).

In the competitive accretion model, star formation is regulated by the global collapse of a much larger cloud, initially containing gas of several thousand M_{\odot} . The material that ends up as stars is gathered during the star-formation process from various parts of the parent cloud. The cores compete for the remaining gas and there are strong interactions among them. This scenario predicts that massive stars form at the cluster center where more massive inflow can occur than in the outer regions (Bonnell et al. 2001; Krumholz & Bonnell 2009).

Regardless of which mechanism works, gravitational inflow is a key process to initiate star formation and to control the evolution of densities in the protostellar envelope. Therefore, characterizing this inflow process is important for a better understanding of high-mass star formation. One observational signature of inflow motion is a ‘blue profile’, a general prediction for a cloud collapsing model (e.g. Shu 1977). This blue profile is an asymmetric line feature that appears in an optically thick line profile with a self-absorption dip and a blue peak stronger than a red peak. The emission of an optically thin line peaks near the absorption dip of the optically thick line.

There have been many attempts to examine the inflow signature in massive star-forming regions in recent years. After Wu & Evans (2003) found statistically significant blue excess (the number of blue profile minus that of red profile in units of the total number of sample) in the blue profile in the HCN $J=3-2$ line toward early phase of HII regions where star-forming activity still appears, the number of studies has been increasing. For example, Reiter et al. (2011a) carried out HCO⁺ $J=3-2$ line observations toward similar regions of Wu & Evans (2003). They noted that every source with the blue asymmetry

in the HCO^+ $J=3-2$ line also has the blue profile in the HCN $J=3-2$ line, and confirmed that the HCN $J=3-2$ line is a better inflow tracer. Rygl et al. (2013) performed the HCO^+ $J=1-0$, $4-3$, and CO $J=3-2$ line observations toward a sample of clumps in clouds with high extinctions, and they concluded that among the three transitions, the HCO^+ $J=1-0$ line is the most sensitive to detect inflowing motions. In addition, Fuller et al. (2005) reported significant excess of blue profiles toward HMPOs in the HCO^+ $J=1-0$, $3-2$, and $4-3$ transitions and H_2CO $2_{12}-1_{11}$ line.

In addition, there have been several previous studies dealing with evolutionary tendency of inflow motion. For example, Wu et al. (2007) showed dramatic increase of blue excess in the HCO^+ $J=1-0$ line with evolution from HMPOs to UCHIIs. Other studies have found different results. Purcell et al. (2006) revealed equal numbers of red and blue profiles of the HCO^+ $J=1-0$ line toward HMPOs and UCHIIs, and found blue excess only in IRDCs, indicating active inflow motion occurring in the early phase of star formation. Recently, an extensive inflow survey toward 405 compact sources classified into prestellar, protostellar and UCHII regions was performed in the HCO^+ $J=1-0$ and HNC $J=1-0$ lines (He et al. 2015). They suggested that the HCO^+ $J=1-0$ line is better to trace inward motion and found that the blue excess declines with evolutionary stage. With a higher transition of HCO^+ , the opposite tendency appears. In the HCO^+ $J=4-3$ study by Klaassen et al. (2012), 12 out of 22 UCHIIs show the blue asymmetric line profile while only 3 blue sources are detected among 12 HMPOs. They attribute this lower occurrence of blue profiles in HMPOs to the beam dilution effect.

Except for the study of Wu et al. (2007), all of these results regarding HCO^+ $J=1-0$ line can be summarized as follows; (1) the HCO^+ $J=1-0$ transition is likely to be the most sensitive inflow tracer. (2) The blue excess measured with this line intensity decreases with evolution of the massive star-forming regions, suggesting that the younger the sources are,

the easier to detect inflow with this tracer. (3) This observing trend, however, can appear differently with the higher transition lines.

However, many of those studies mainly used the HCO^+ transitions as an inflow tracer or dealt with limited phases of massive star formation. However, different line transitions at different molecular species must be tested because inflow could be associated with various excitation conditions. In this study, we search for inflow candidates toward various evolutionary stages related to massive star formation (IRDCs, HMPOs, and UCHIIs) using the HCN and HNC $J=1-0$ lines. This paper is organized as follows. The details about source selection and observations are provided in §2. Analyses for asymmetric profiles are presented in §3. The discussion for inflow candidates is provided in §4. The main results are summarized in §5.

2. Observation

2.1. Target Selection

After Rathborne et al. (2006) identified 190 compact cores in the 1.2 mm continuum images of the 38 darkest IRDCs, Chambers et al. (2009) classified them as ‘quiescent’ prestellar cores (qIRDCc) and ‘active’ protostellar cores (aIRDCc). aIRDCc show both 4.5 and 24 μm infrared emission which is the signature of star-forming activities, while qIRDCc contain neither emission. We adopted 19 qIRDCc and 35 aIRDCc from the catalog of Chambers et al. (2009) as our IRDC targets. We selected 69 HMPOs from the catalogs of Sridharan et al. (2002) and Molinari et al. (1996) and 54 UCHIIs from the catalogs of Wood & Churchwell (1989) and Kurtz et al. (1994). The details about selection criteria are provided in Jin et al. (2015). Consequently, our sample consists of 54 IRDCs (19 qIRDCc and 35 aIRDCc), 69 HMPOs, and 54 UCHIIs.

2.2. Observation

The $J=1-0$ transitions of HCN and HNC and their isotopic lines (Table 1) were observed in 2012–2013 using the Korean VLBI Network (KVN) 21m telescope at the Yonsei and Ulsan stations (Kim et al. 2011; Lee et al. 2011). The main-beam efficiencies are 0.43 and 0.37 for the KVN Yonsei and Ulsan telescopes, respectively, and the beam sizes of both telescopes are $32''$. All the lines were observed with the position switching mode and their intensities were calibrated on the T_A^* scale by the standard chopper wheel method. The focus and pointing were adjusted by observing strong SiO maser sources every one to two hours. The system temperature ranged from 170 K to 280 K. The rest frequencies, dipole moments, and relative weights of the hyperfine components of the observed lines are summarized in Table 1. All spectra were reduced using CLASS in the GILDAS software package, and the reduced line spectra have velocity resolution of 0.21 km s^{-1} .

3. Analysis & Results

To select sources for analysis of inflow signatures, first, we used a 3σ -detection criterion for each line. After that, some sources are excluded by eye if they are suspected to have multiple velocity components in a line of sight. Specifically, eight IRDC cores are excluded in the analysis of HCN $J=1-0$. The hyperfine components are strongly self-absorbed and blended each other, making it hard for the lines to be exploited in the inflow analysis. In addition, there are additional emission components that cannot be solely explained by the combination of self-absorption and line blending effects in some sources. Finally, 12 IRDCs, 26 HMPOs and 23 UCHIIs are selected for the HCN and H^{13}CN line analysis while 25 IRDCs, 28 HMPOs and 23 UCHIIs are selected for the analysis of the HNC and HN^{13}C lines. The information of the sources selected for analysis is listed in Table 2.

According to Wu & Evans (2003), the inflow proceeds at a relatively low velocity so that its observational signature can be easily masked by other mechanism or a beam dilution effect. However, all our samples that are listed in the SCUBA legacy catalogue have larger effective radii than half of our beam size in the $850\mu\text{m}$ continuum (Di Francesco et al. 2008; Jin et al. 2015), indicating that the emission is not likely beam-diluted. The HCN and HNC line emissions are known to be well correlated with the dust emission (Wu et al. 2010; Reiter et al. 2011b).

The general signature of inflow is the so called ‘blue profile’. This is an asymmetric line feature with a self-absorption dip where the blue peak is stronger than the red peak, while an optically thin line must peak near the dip of the optically thick line. In this case, the ratio of the blue peak to the red peak ($T(B)/T(R)$) can be one measure for the line asymmetry. However, depending on the opacity of the line, the blue profiles can show other features, for example, a single blue peak with red shoulder or a blue-skewed single peak. Figure 1–2 show the various features of blue profiles in the HCN and HNC $J=1-0$ lines, respectively, ranging from a clearly self-absorbed blue profile to a blue-skewed profile.

In low-mass star forming regions, Mardones et al. (1997) have suggested δv as an alternative measure of the blue profile for these blue skewed lines, which is defined as a difference between the line central velocity of an optically thick line (v_{thick}) and that of an optically thin line (v_{thin}), in units of the line width of the optically thin line (Δv_{thin})

$$\delta v = \frac{v_{\text{thick}} - v_{\text{thin}}}{\Delta v_{\text{thin}}}. \quad (1)$$

A line can be identified as blue/red profile if the difference between v_{thick} and v_{thin} is greater than a quarter of Δv_{thin} . That is, a blue profile would have $\delta v < -0.25$ while a red profile would have $\delta v > 0.25$ (Mardones et al. 1997). However, it is important to note that adopting the same boundaries on δv for these high-mass objects actually demands a larger velocity shift than for the low-mass sources because the molecular lines towards

these high-mass samples are significantly broader (Fuller et al. 2005).

We measured the line asymmetries of all the detected sources using the δv analysis under the assumption that both H^{13}CN and HN^{13}C lines are optically thin. The optical depth for each line was obtained by adopting the values of Jin et al. (2015) or by following the same analysis described therein. The resulting mean value for each line was less than 0.12 in all the evolutionary stages. For the HCN and H^{13}CN $J=1-0$ spectra consisting of three apparent hyperfine lines, the strongest hyperfine component ($F=2-1$) is adopted as a standard for δv calculation. All the line central velocities (v_{thick} , v_{thin}) and line widths (Δv_{thin}) are determined from multiple-Gaussian fitting. The HNC $J=1-0$ line also has a hyperfine structure, but the splitting is too small ($\sim 0.7 \text{ km s}^{-1}$; van der Tak et al. (2009)) to perform the multiple Gaussian fitting. As a result, the values of δv were calculated in the same manner, but all the line parameters are measured with a single-Gaussian fitting.

As mentioned above, the strongest hyperfine component ($F=2-1$) is mainly used for the HCN $J=1-0$ transition in the δv analysis because this component is detected toward all sources, unlike other weak components, so that we can maximize the sample number for our analysis. Prior to adopting the $F=2-1$ hyperfine component as standard, we derived the correlations among δv values not only measured from the Gaussian fitting for each HCN hyperfine component but also measured by fitting the whole hyperfine structure simultaneously. As presented in Figure 3, they show tight correlations in the confidence level above 99 %. Therefore, $F=2-1$ can be representative for all hyperfine components in our analysis. The observed line parameters and derived δv are listed in Tables 3 and 4. Figures 4 and 5 show the distribution of δv derived from HCN and HNC lines, respectively. The sources located in the left side of the blue dashed line have blue profiles, while those on the right side of the red dashed line have red profiles.

An asymmetric profile may also be induced by other mechanism (e.g., rotation and outflow). If this is the case, a large sample with a random distribution of angles between the axis and the line of sight will not produce an excess of one type of profile (Wu & Evans 2003). So the concept of the “blue excess” was introduced by Mardones et al. (1997) to quantify the statistics of the line asymmetry in a survey:

$$E = \frac{N_{\text{blue}} - N_{\text{red}}}{N_{\text{total}}} \quad (2)$$

where N_{blue} and N_{red} are the numbers of blue and red profiles in the total samples (N_{total}). These statistical results are summarized in Table 5.

4. Discussion

Values of the blue excess derived from the HCN $J=1-0$ line for IRDCs, HMPOs, and UCHIIs (0.42, 0.15, and 0.30, respectively) are larger than those derived from the HNC $J=1-0$ line (0.28, -0.07, and 0.00, respectively). In the HCN spectra, a prevalence of blue profiles relative to red profiles is found in every evolutionary stage, with the IRDCs showing the largest blue excess (Figure 4). In contrast, the distribution of the δv derived from the HNC line is relatively centered on neutral profiles, excepting for IRDCs (Figure 5).

We performed a binomial test and calculated the probability P that the one type of excess is induced by chance. The binomial distribution is described as follows

$$P = \binom{n}{k} p^k (1-p)^{(n-k)}, \quad (3)$$

where n is the total number of trials, k is the number of successes, and p is the success probability. In this case, n is the total number of sources, k is the number of the blue sources, and the success probability $p=0.5$ if the distribution shows no bias toward red or blue.

Then the possibility that the number of blue sources is equal to or higher than the observed

number by chance can be calculated by adding all possibilities $P(n, k, p) + P(n, k + 1, p) + \dots$ until $k = n$. A small value of P indicates that it is unlikely for a blue excess to arise by chance (Rygl et al. 2013). All resulting values of E and P are listed in Table 5. The E of the HCN line is statistically significant with a sufficiently low probability P throughout all evolutionary phases. In the case of the HNC line, in contrast, such a significant value of E appears only in the IRDC phases. The fact that the IRDCs show the highest blue excess in both inflow tracers indicates that the most active inflow occurs in the early phase of massive star formation, even though the characteristics of blue profile largely depend on the suitable combination of optical depth and critical density. It should be noted that the small sample size of HCN sources in IRDCs would bring about statistical instability in calculating blue excess E . Nevertheless, the probability P as low as 6 % indicates that the prevalence of blue profile is not likely to occur by chance. In addition, the HNC line also shows significant excess to blue in the IRDCs.

4.1. The astrochemical effect on inflow tracer

These results suggest that the HCN $J=1-0$ line is a better inflow tracer than the HNC $J=1-0$ line in massive star-forming regions. The δv values of the sources detected in both inflow tracers are plotted in Figure 6. The sources located outside the blue/red dashed lines are considered as the blue/red profiles, while the sources located inside those lines are regarded as neutral profiles. Many sources blue in HCN are neutral in HNC, but not vice versa, indicating the HNC is less appropriate to trace inflow motion. We attribute this to an astrochemical effect that reduces the abundance, hence, the optical depth of HNC.

Jin et al. (2015) have found that HCN/HNC abundance ratio increases while the optical depth of HN^{13}C decreases as sources evolve from IRDC to UCHIIs, even though both HCN and HNC are mainly formed in equal measure by dissociative recombination (Mendes et al.

2012). One suggested reason for this phenomenon is a neutral–neutral reaction where HNC is selectively consumed at high temperatures ($T_K \geq 24$ K; Hirota et al. (1998)). Hirota et al. (1998) showed that the HCN abundances in the high kinetic temperature regions (OMC-1 cores) are comparable to those in the dark cloud cores whereas the HNC abundances decrease as the temperature rises. By this astrochemical effect, the opacity of the HNC line would decrease as an object evolves so that the line cannot trace inflow motion well; an inflow profile appears in lines sufficiently opaque (Myers et al. 1996). In Figure 6, a significant number of HMPO and UCHII sources are bluer in HCN than HNC. On the contrary, the HNC line is rather bluer in the IRDCs, and this opposite tendency is more obvious in qIRDCc than aIRDCc, supporting our scenario again. The qIRDCc is considered to be in the earlier phase (Chambers et al. 2009) and show the smaller value of the HCN/HNC abundance ratio than aIRDCc (Jin et al. 2015). This result spotlights the importance of regarding chemistry when studying dynamics of star–forming regions.

4.2. Comparison with previous studies

There have been many attempts to examine the inflow signature as mentioned in §1. Some of those studies have suggested the HCO^+ $J=1-0$ line as the best inflow tracer in massive star–forming regions. We compare our results not only with the previous inflow surveys using the HCO^+ $J=1-0$ line but also with the study using a higher transition line of HCN.

In the HCO^+ $J=1-0$ line, IRDCs seem to undergo the most detectable active inflow process (Purcell et al. 2006; Rygl et al. 2013; He et al. 2015) whereas sources in more evolved phases such as HMPOs and UCHIIs show less inflow as indicated by smaller values of the blue excess. For example, Purcell et al. (2006) reported the blue excess as low as 0.02 toward these evolved samples, and He et al. (2015) found the decreasing tendency of

the blue excess with evolution from IRDCs to UCHIIIs. The blue excess that we observed with the HCN $J=1-0$ line are comparable with their values for each evolutionary stage with the largest value in IRDCs. This indicates that the HCN $J=1-0$ line is as sensitive as the HCO^+ $J=1-0$ line in high-mass star forming regions.

For a higher transition of HCN, Wu & Evans (2003) surveyed inflow motion using the HCN $J=3-2$ line. They reported the blue excess of 0.21 in the sources consisting of the 28 HII regions where the star-forming activity still appears. This value is much smaller than the blue excess for our UCHIIIs sample (0.30 for 23 UCHIIIs), showing that the 1-0 transition line of HCN traces the inflow motion better than the higher transition line. This result is consistent with the result of Fuller et al. (2005); the lower transition lines of HCO^+ show the more inflow signature. They observed the HCO^+ $J=1-0$, 3-2, and 4-3 transitions toward HMPOs and found the highest blue excess in the $J=1-0$ line. This result may be related to the gas motion (i.e., velocity profile) that the high energy level transitions trace; the higher transition lines emit from the hotter and denser central region. According to a model of collapsing cloud in massive star-forming regions, the velocity gradient at the central region is too large to make the self-absorption feature in high energy transitions (Smith et al. 2013).

4.3. Global collapse?

An interesting feature in double-peaked HNC spectra is that the absorption dips in 6 out of 7 blue sources are red-shifted relative to the systemic velocities. For the sources whose lines are strongly self-absorbed, the asymmetries of the spectra are determined using the $T(B)/T(R)$ parameter. The fluxes of the two peaks are measured by the double-Gaussian fitting, and if the differences between the peaks are larger than the 3σ noise level, we classify them into blue/red profiles otherwise neutral profile. Some sources suspected to

have a wing-like structure, however, couldn't be fitted by the double-Gaussians directly even though an obvious self-absorption feature appears. Those lines are fitted after masking the wing-like structures. After that, we compare the velocity of the absorption dip (v_{dip}) with the systemic velocity determined from the HN^{13}C line. The v_{dip} is identified as a velocity at the lowest flux in the absorption dip by cursor. If the velocity deviation of the absorption dip exceeds three times the measurement error of the systemic velocity, the line is considered to have a shifted dip. The asymmetry parameters ($T(B)/T(R)$), the velocities of the absorption dips (v_{dip}) of the HNC $J=1-0$ line and central velocities of the HN^{13}C $J=1-0$ line (v_{thin}) are listed in Table 4. We also tried to perform the same analysis in the HCN spectra. However, the double-Gaussian fitting was not reliable because of the combination of the line blending effects among the hyperfine components and the self-absorption.

According to the above analysis, 6 out of 7 blue sources have absorption dips red-shifted relative to their systemic velocity (Figure 7). If considering turbulent core accretion model, the star formation occurs in quasi-equilibrium molecular cloud where inflow occurs in localized regions. This would make the absorption dip at the source velocity. However, if the cloud clumps form in global collapse as described in the competitive accretion model, even the outer larger region takes part in the inflowing process, making the absorption dip red-shifted. Therefore, these red-shifted absorption dips detected in our sources may indicate global collapse candidates. Actually, Smith et al. (2013) calculated the line profiles of HCO^+ in a core following the competitive accretion formalism and frequently found non-central self-absorption dip. However, depending on optical depth, red-shifted absorption dip can be also induced by the absorption in the inner collapsing regions. Mapping observations with better resolution are needed to rule out this possibility.

5. Summary

To understand the gravitational inflow taking place in high-mass star formation, we surveyed 54 IRDC cores, 69 HMPOs, and 54 UCHIIs in the HCN $J=1-0$ and HNC $J=1-0$ lines.

(1) We found a statistically significant blue excess of the HCN line for every evolutionary phase (0.42, 0.15, and 0.30 for IRDCs, HMPOs, and UCHIIs, respectively). These are comparable to the values derived using other inflow tracers, including HCO^+ $J=1-0$, known to be one of the best inflow tracers. This indicates the HCN line is a good tracer of gravitational inflow.

(2) With the HNC line, the blue profile appears significant only in IRDCs. We concluded that this line is not appropriate to trace inflow motion in evolved stages of massive star formation because of the HNC abundance (and thus, its optical depth) decreases at high temperatures. This result spotlights the importance of considering chemistry in studying dynamics of massive star-forming regions.

(3) The fact that IRDCs show the highest blue excess in both inflow tracers indicates that the IRDC phase is undergoing the most active inflow process. This result is consistent with a general prediction of inflow process where the younger sources are expected to be more actively inflowing onto the central source. However, the UCHIIs is also likely inflowing matters yet.

(4) We found that the absorption dips of the HNC $J=1-0$ spectra are red-shifted relative to the systemic velocities in 6 out of 7 blue sources. These red-shifted absorption dips suggest that the clumps are in global collapse. Mapping observations with better angular resolutions are needed to examine this feature in more detail.

Acknowledgements

We are grateful to all staff members in KVN who helped to operate the telescope. The KVN is a facility operated by the Korea Astronomy and Space Science Institute. This work was supported by the Basic Science Research Program through the National Research Foundation of Korea (NRF) (grant No. NRF-2015R1A2A2A01004769) and the Korea Astronomy and Space Science Institute under the R &D program (Project No. 2015-1-320-18) supervised by the Ministry of Science, ICT and Future Planning.

REFERENCES

- Bodenheimer, P. H. 2011, Principles of star formation
- Beuther, H., Schilke, P., Menten, K.M., et al. 2002, ApJS, 566, 945
- Beuther, H., & Schilke, P. 2004, Science, 303, 1167
- Bhattacharya, B. N., & Gordy, W. 1960, Phys. Rev., 119, 144
- Blackman, G. L., Brown, R. D., Godfrey, P. D., & Gunn, H. I. 1976, Nature, 261, 395
- Bonnell, I. A., Bate, M. R., Clarke, C. J., & Pringle, J. E. 2001, MNRAS, 323, 785
- Chambers, E.T., Jackson, J.M., Rathborne, J.M., & Simon, R. 2009, ApJS, 181, 360
- Choi, M. 2002, ApJ, 575, 900
- Di Francesco, J., Johnstone, D., Kirk, H. M., MacKenzie, T., & Ledwosinska, E. 2008, ApJS, 175,277
- Egan, M.P., Shimpman, R.F., Price, S.D., Carey, S.J., & Clark, F.O. 1998, ApJ, 494, L199
- Fuller, G. A., Williams, S. J., & Sridharan, T. K. 2005, A&A, 442, 949
- Gregersen, E. M., Evans, N. J., II, Zhou, S., & Choi, M. 1997, ApJ, 484, 256
- He, Y.-X., Zhou, J.-J., Esimbek, J., et al. 2015, MNRAS, 450, 1926
- Hirota, T., Yamamoto, S., Mikami, H. et al. 1998, ApJ, 503, 717
- Jin, M., Lee, J.-E., & Kim, K.-T. 2015, ApJS, 219, 2
- Kim, K.-T., & Koo, B.-C. 2001, ApJ, 549, 979
- Kim, K.-T., Byun, D.-Y., Je, D.-H., et al. 2011, JKAS., 44, 81

- Klaassen, P. D., Testi, L., & Beuther, H. 2012, *A&A*, 538, A140
- Krumholz, M. R., & Bonnell, I. A. 2009, *Structure Formation in Astrophysics*, 288
- Krumholz, M. R., & Tan, J. C. 2007, *ApJ*, 654, 304
- Kurtz, S., Churchwell, E., & Wood, D.O.S. 1994, *ApJS*, 91, 659
- Lee, S.-S., Byun, D.-Y., Oh, C. S., et al. 2011, *PASP*, 123, 1398
- Mardones, D., Myers, P.C., Tafalla, M., & Wilner, D.J. 1997, *ApJ*, 489, 719
- McKee, C. F. & Ostriker, E. C. 2007, *ARA&A*, 45, 565M
- McKee, C. F., & Tan, J. C. 2003, *ApJ*, 585, 850
- Mendes, M.B., Buhr, H., Berg, M.H., et al. 2012, *ApJ*, 746L, 8M
- Molinari, S., Brand, J., Cesaroni, R., & Palla, F. 1996, *A&A*, 308, 573
- Molinari, S., Brand, J., Cesaroni, R., & Palla, F. 2000, *A&A*, 355, 617
- Motte, F., Andre, P., & Neri, R. 1998, *A&A*, 336, 150
- Myers, P. C., Mardones, D., Tafalla, M., Williams, J. P., & Wilner, D. J. 1996, *ApJ*, 465, L133
- Purcell, C. R., Balasubramanyam, R., Burton, M. G., et al. 2006, *MNRAS*, 367, 553
- Rathborne, J.M., Jackson, J.M., & Simon, R. 2006, *ApJ*, 641, 389
- Reiter, M., Shirley, Y. L., Wu, J., et al. 2011, *A&A*, 740, 40
- Reiter, M., Shirley, Y. L., Wu, J., et al. 2011 *ApJS*, 195, 1
- Rygl, K. L. J., Wyrowski, F., Schuller, F., & Menten, K. M. 2013, *ApJ*, 549, A5

Shu, F. H. 1977, ApJ, 214, 488

Simon, R., Jackson, J.M., Rathborne, J.M., & Chambers, E.T. 2006a, ApJ, 639, 227

Simon, R., Rathborne, J.M., Shah, R.Y., Jackson, J.M., & Chambers, E.T. 2006b, ApJ, 653, 1325

Smith, R. J., Shetty, R., Beuther, H., Klessen, R. S., & Bonnell, I. A. 2013, ApJ, 771, 24

Sridharan, T.K., Beuther, H., Schilke, P., Menten, K.M., & Wyrowski, F 2002, ApJ, 566, 931

Thompson, M.A., Hatchell, J., Walsh, A.J., Macdonald, G.H., & Millar, T.J. 2006, A&A, 453, 1003

van der Tak, F. F. S., Müller, H. S. P., Harding, M. E., & Gauss, J. 2009, A&A, 507, 347

Wood, D.O.S., & Churchwell, E. 1989, ApJS, 69, 831

Wu, J., & Evans, N.J. 2003, ApJ, 592, L79

Wu, Y., Henkel, C., Xue, R., Guan, X., & Miller, M. 2007, ApJ, 669, L37

Wu, J., Evans, N. J., II, Shirley, Y. L., & Knez, C. 2010, ApJS, 188, 313-357

Zinnecker, H., & Yorke, H. W. 2007, ARA&A, 45, 481

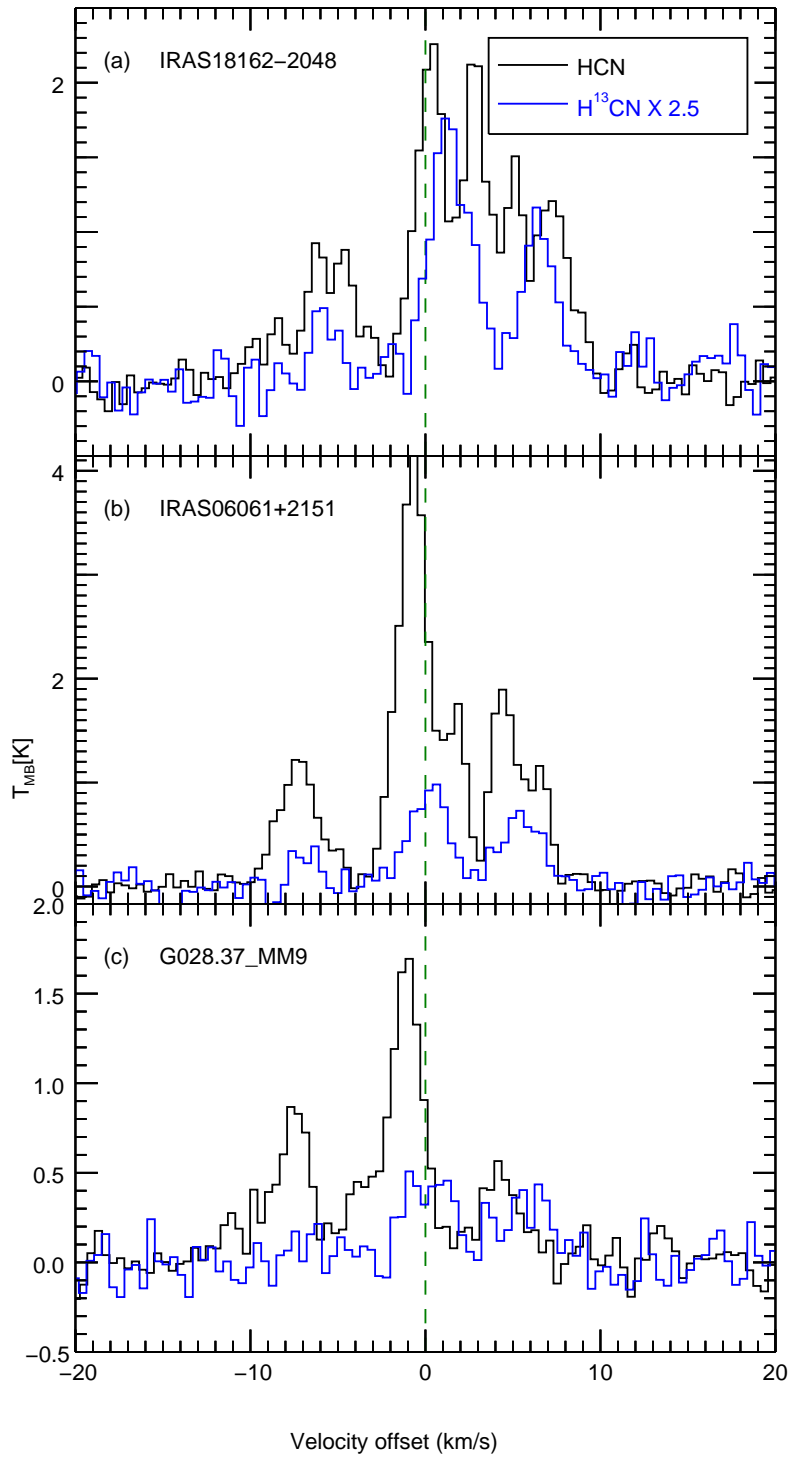


Fig. 1.— Various features of blue profiles in the HCN $J=1-0$ line. Both lines are plotted with the velocity relative to the optically thin line’s central velocity (green dashed lines).

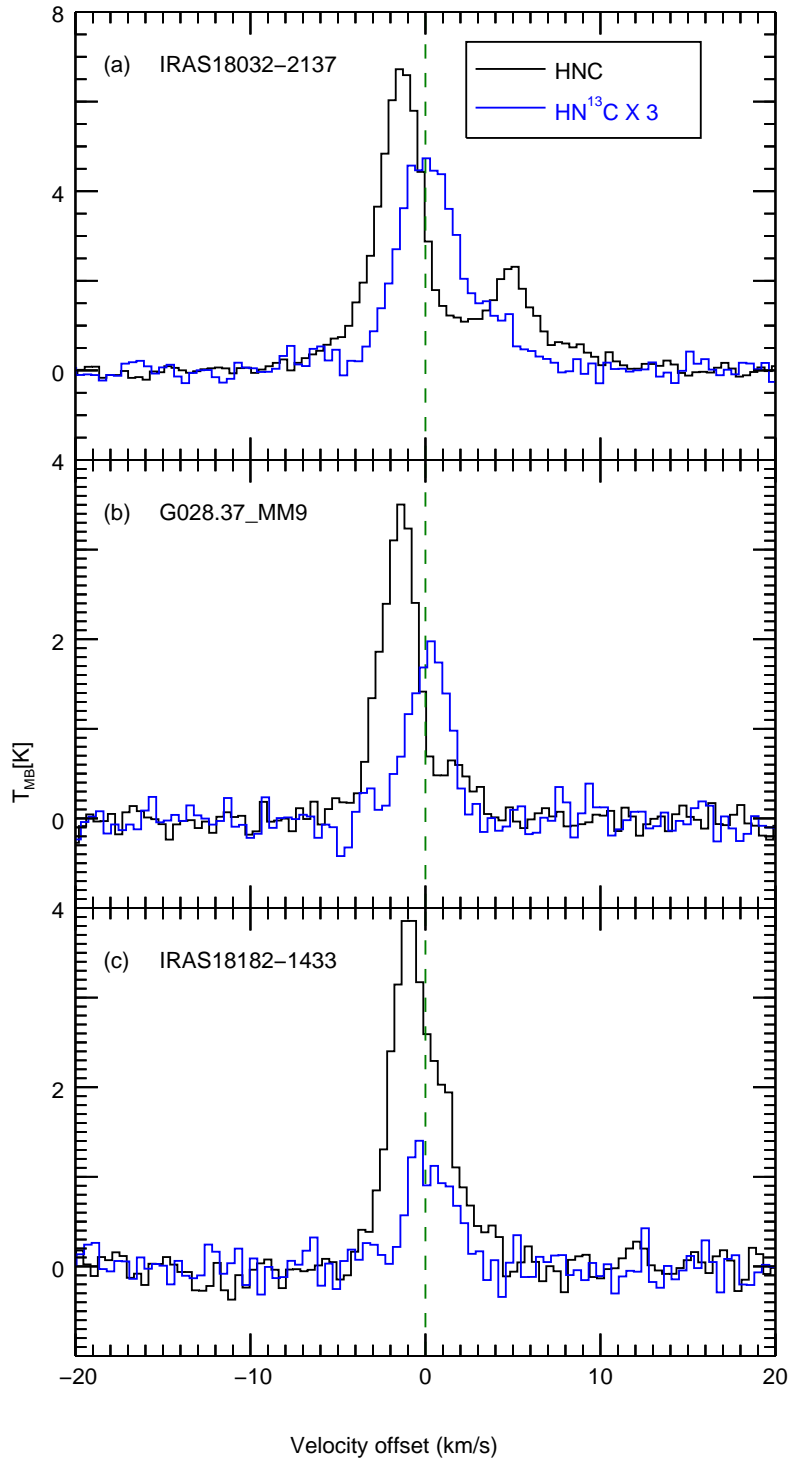


Fig. 2.— Various features of blue profiles in the HNC $J=1-0$ line. Both lines are plotted with the velocity relative to the optically thin line’s central velocity (green dashed lines).

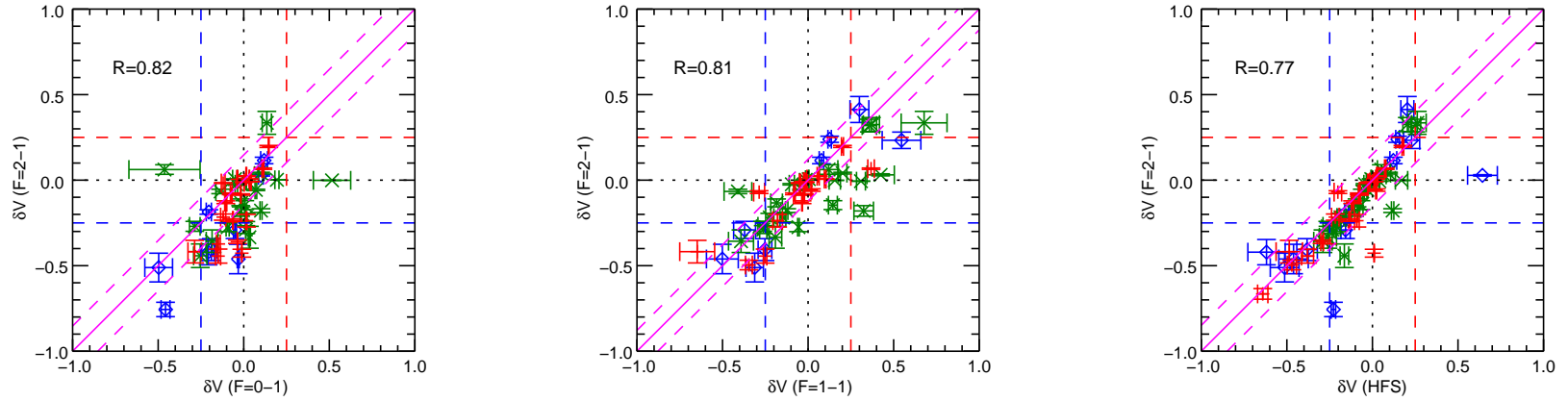


Fig. 3.— Comparison the δv values derived from the main hyperfine component ($F=2-1$) of the HCN $J=1-0$ line with the values derived from the other hyperfine satellites (left and medium panel) and from the all three hyperfine components at once (right panel). IRDC cores, HMPOs, and UCHIIs are indicated by diamonds, times, and crosses, respectively. The solid line is the line of perfect correlation and the dotted lines indicate $1-\sigma$ from the line. The Pearson correlation coefficients (R) are given in the upper left corner of each panel, and p -values for all correlations are extremely small. The number of samples in each box is 50, 49, and 61, respectively, from left to right. One HMPO (IRAS23140+6121) whose value is ($\delta v (F=0-1)=-1.606$, $\delta v (F=2-1)=1.710$) is not presented in the first panel.

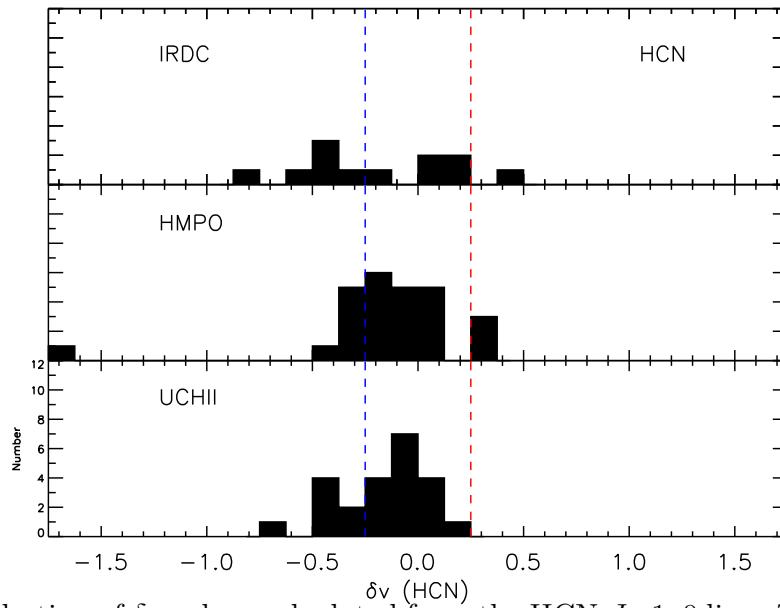


Fig. 4.— Distribution of δv values calculated from the HCN $J=1-0$ line. The sources located outside the blue/red dashed lines can be considered as blue/red profiles, whereas the sources inside the blue and red dashed lines are neutral profiles. The top, middle, and bottom panels represent results from 12 IRDC cores, 26 HMPOs, and 23 UCHIIs, respectively.

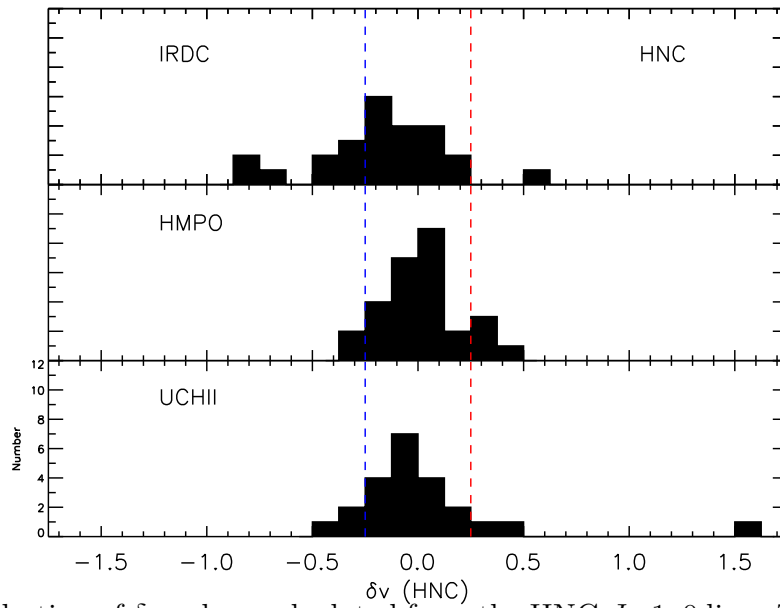


Fig. 5.— Distribution of δv values calculated from the HNC $J=1-0$ line. The sources located outside the blue/red dashed lines can be considered as blue/red profiles, whereas the sources inside the blue and red dashed lines are neutral profiles. The top, middle, and bottom panels represent results from 25 IRDC cores, 28 HMPOs, and 23 UCHIIs, respectively.

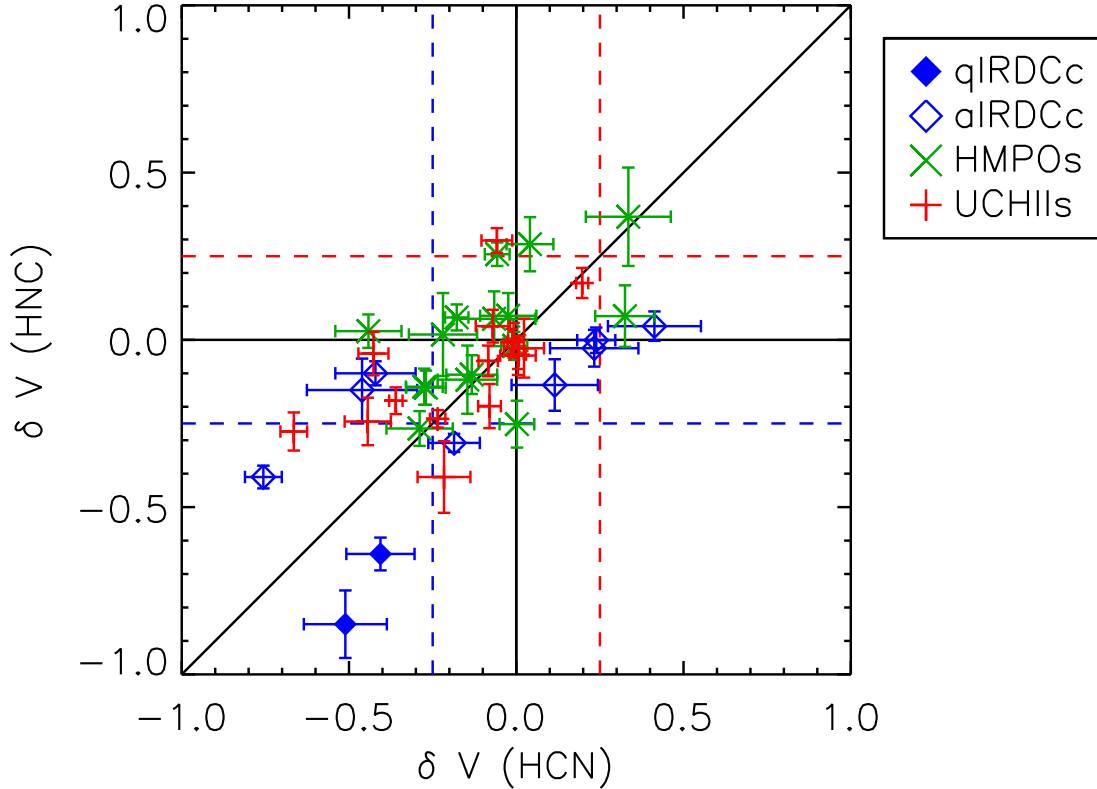


Fig. 6.— Comparison of δv values between HNC and HCN. Only the sources where we can analyze both inflow tracers are plotted here. IRDC cores, HMPOs, and UCHIIs are indicated by diamonds, times, and crosses, respectively. Here IRDC cores are divided into quiescent ones (qIRDCc, filled diamonds) and active ones (aIRDCc, open diamonds), depending on star-forming activity. The sources located outside the blue/red dashed lines can be considered as blue/red profiles. One UCHII source whose value is $(-0.137, 1.524)$ is not presented here.

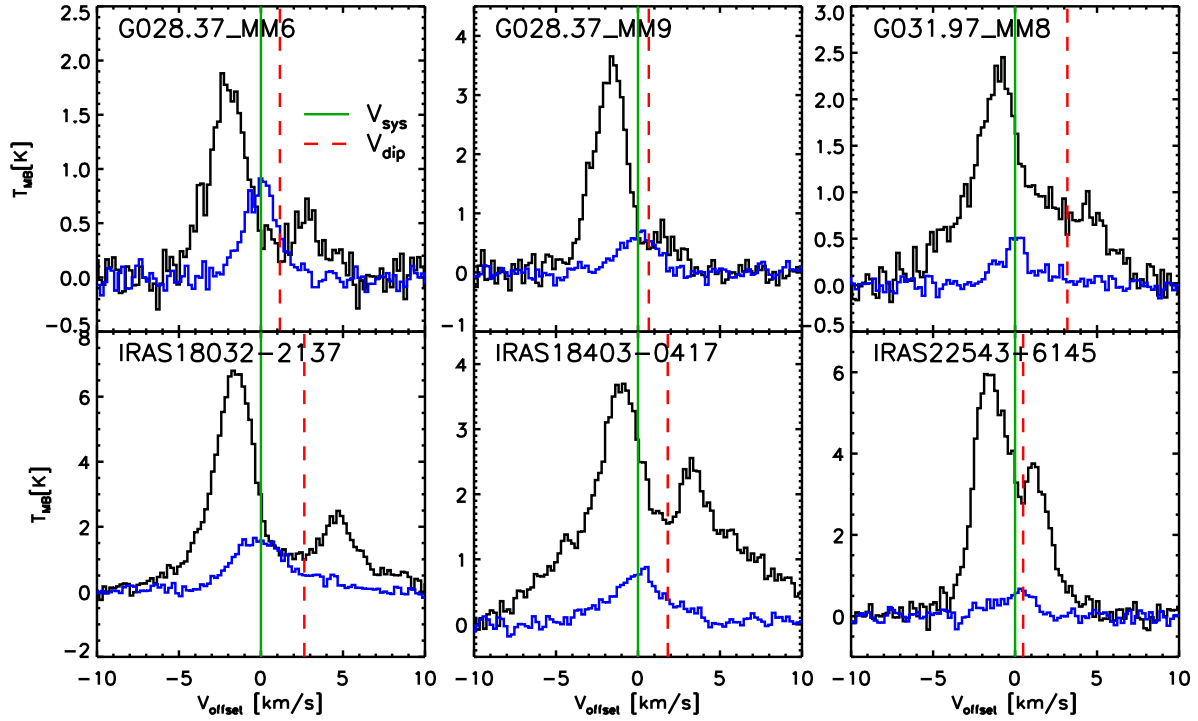


Fig. 7.— The blue profile with red-shifted absorption dip in the HNC $J=1-0$ line. Both HNC (black) and HN¹³C (blue) lines are plotted with the velocity relative to the systemic velocity (green solid lines). Red dashed line represents the dip position.

Table 1. Observed Lines

Molecule	Transition	ν [MHz]	μ [D]	S_{ul}^{a}
HCN	$J=1-0, F=2-1$	88630.42	2.99 ^b	3
	$J=1-0, F=1-1$	88631.85		5
	$J=1-0, F=0-1$	88633.94		1
H ¹³ CN	$J=1-0, F=2-1$	86338.77	2.99 ^b	3
	$J=1-0, F=1-1$	86340.18		5
	$J=1-0, F=0-1$	86342.27		1
HNC	$J=1-0$	90663.57	3.05 ^c	
HN ¹³ C	$J=1-0$	87090.85	3.05 ^c	

Note. — ^a Relative weights of the hyperfine components. ^b Bhattacharya & Gordy (1960). ^c Blackman et al. (1976).

Table 2. Source information

Classification	Source name	R.A.	Decl.	l	b	D_{far}	D_{near}	inflow tracer
		J(2000.0)	J(2000.0)	($^{\circ}$)	($^{\circ}$)	(kpc)	(kpc)	
qIRDCc	G028.37_MM9	18:42:46.7	-04:04:08	28.32	0.07	5.0	...	HCN, HNC
	G031.97_MM9	18:49:31.6	-00:46:30	32.02	0.07	6.9	...	HNC
	G035.39_MM5	18:57:08.8	+02:08:09	35.48	-0.30	2.9	...	HCN, HNC
aIRDCc	G015.31_MM3	18:18:45.3	-15:41:58	15.28	-0.09	3.2	...	HNC
	G022.35_MM1	18:30:24.4	-09:10:34	22.38	0.45	4.3	...	HCN
	G023.60_MM1	18:34:11.6	-08:19:06	23.57	0.01	3.9	...	HNC
	G023.60_MM6	18:34:18.2	-08:18:52	23.59	-0.01	3.9	...	HNC
	G024.60_MM1	18:35:40.2	-07:18:37	24.63	0.15	3.7	...	HNC
	G028.37_MM4	18:42:50.7	-04:03:15	28.34	0.06	5.0	...	HNC
	G028.37_MM6	18:42:49.0	-04:02:23	28.36	0.07	5.0	...	HNC
	G030.97_MM1	18:48:21.6	-01:48:27	30.97	-0.14	5.1	...	HCN, HNC
	G031.97_MM1	18:49:36.3	-00:45:45	32.04	0.06	6.9	...	HCN, HNC
	G031.97_MM8	18:49:29.1	-00:48:12	32.00	0.07	6.9	...	HNC
	G033.69_MM4	18:52:56.4	+00:43:08	33.74	0.00	7.1	...	HCN, HNC
	G033.69_MM5	18:52:47.8	+00:36:47	33.63	-0.02	7.1	...	HCN, HNC
	G034.43_MM1	18:53:18.0	+01:25:24	34.41	0.24	3.7	...	HNC
	G034.43_MM3	18:53:20.4	+01:28:23	34.46	0.25	3.7	...	HNC
	G034.43_MM4	18:53:19.0	+01:24:08	34.39	0.22	3.7	...	HCN, HNC
	G035.39_MM7	18:57:08.1	+02:10:50	35.52	-0.27	2.9	...	HCN
	G035.59_MM3	18:57:11.6	+02:16:08	35.61	-0.24	2.9	...	HNC
	G038.95_MM3	19:04:07.4	+05:09:44	38.97	-0.46	2.7	...	HNC
	G038.95_MM4	19:04:00.6	+05:09:06	38.95	-0.44	2.7	...	HNC
	G048.65_MM1	19:21:49.7	+13:49:30	48.67	-0.30	2.5	...	HCN, HNC
G048.65_MM2	19:21:47.6	+13:49:22	48.66	-0.30	2.5	...	HNC	

Table 2—Continued

Classification	Source name	R.A.	Decl.	l	b	D_{far}	D_{near}	inflow tracer
		J(2000.0)	J(2000.0)	($^{\circ}$)	($^{\circ}$)	(kpc)	(kpc)	
	G053.25_MM4	19:29:34.5	+18:01:39	53.25	0.05	1.9	...	HCN, HNC
	G053.25_MM6	19:29:31.5	+17:59:50	53.22	0.05	1.9	...	HCN, HNC
	G053.31_MM2	19:29:42.1	+18:03:57	53.30	0.05	2.0	...	HNC
HMPO	IRAS00117+6412	00:14:27.7	+64:28:46	118.96	1.89	1.8	...	HCN
	IRAS05358+3543	05:39:10.4	+35:45:19	173.48	2.43	1.8	...	HCN, HNC
	IRAS05373+2349	05:40:24.4	+23:50:54	183.72	-3.66	1.2	...	HCN, HNC
	IRAS18024-2119	18:05:25.4	-21:19:41	8.83	-0.03	0.1	...	HNC
	IRAS18089-1732	18:11:51.3	-17:31:28	12.89	0.49	13.0	3.6	HNC
	IRAS18102-1800	18:13:12.2	-17:59:35	12.63	-0.02	14.0	2.6	HNC
	IRAS18144-1723	18:17:24.4	-17:22:13	13.66	-0.60	4.3	...	HNC
	IRAS18151-1208	18:17:57.1	-12:07:22	18.34	1.77	3.0	...	HCN, HNC
	IRAS18162-1612	18:19:07.5	-16:11:21	14.89	-0.40	4.9	...	HNC
	IRAS18182-1433	18:21:07.9	-14:31:53	16.58	-0.05	11.8	4.5	HCN, HNC
	IRAS18223-1243	18:25:10.9	-12:42:17	18.66	-0.06	12.4	3.7	HCN, HNC
	IRAS18264-1152	18:29:14.3	-11:50:26	19.88	-0.53	12.5	3.5	HCN, HNC
	IRAS18290-0924	18:31:44.8	-09:22:09	22.36	0.06	10.5	5.3	HNC
	IRAS18308-0841	18:33:31.9	-08:39:17	23.20	0.00	10.7	4.9	HCN
	IRAS18310-0825	18:33:47.2	-08:23:35	23.46	0.07	10.4	5.2	HNC
	IRAS18345-0641	18:37:16.8	-06:38:32	25.41	0.10	9.5	...	HNC
	IRAS18440-0148	18:46:36.3	-01:45:23	30.82	0.27	8.3	...	HCN, HNC
	IRAS18445-0222	18:47:10.8	-02:19:06	30.38	-0.11	9.4	5.3	HCN
	IRAS18447-0229	18:47:23.7	-02:25:55	30.31	-0.21	8.2	6.6	HCN
	IRAS18470-0044	18:49:36.7	-00:41:05	32.11	0.09	8.2	...	HCN, HNC
	IRAS18488+0000	18:51:24.8	+00:04:19	32.99	0.04	8.9	5.4	HNC

Table 2—Continued

Classification	Source name	R.A.	Decl.	l	b	D_{far}	D_{near}	inflow tracer
		J(2000.0)	J(2000.0)	($^{\circ}$)	($^{\circ}$)	(kpc)	(kpc)	
	IRAS18511+0146	18:53:38.1	+01:50:27	34.82	0.35	3.9	...	HNC
	IRAS18527+0301	18:55:16.5	+03:05:07	36.11	0.55	5.26	...	HCN
	IRAS18530+0215	18:55:34.2	+02:19:08	35.47	0.14	8.7	5.1	HCN, HNC
	IRAS19012+0536	19:03:45.1	+05:40:40	39.39	-0.14	8.6	4.6	HCN
	IRAS19035+0641	19:06:01.1	+06:46:35	40.62	-0.14	2.2	...	HCN
	IRAS19220+1432	19:24:19.7	+14:38:03	49.67	-0.46	5.5	...	HNC
	IRAS19410+2336	19:43:11.4	+23:44:06	59.78	0.06	6.4	2.1	HCN
	IRAS19411+2306	19:43:18.1	+23:13:59	59.36	-0.21	5.8	2.9	HCN, HNC
	IRAS19413+2332	19:43:28.9	+23:40:04	59.76	-0.03	6.8	1.8	HCN
	IRAS20126+4104	20:14:26.0	+41:13:32	78.12	3.63	1.7	...	HCN, HNC
	IRAS20216+4107	20:23:23.8	+41:17:40	79.12	2.28	1.7	...	HCN, HNC
	IRAS20293+3952	20:31:10.7	+40:03:10	78.98	0.36	2.0	1.3	HNC
	IRAS20343+4129	20:36:07.1	+41:40:01	80.83	0.57	1.4	...	HCN, HNC
	IRAS22134+5834	22:15:09.1	+58:49:09	103.88	1.86	2.6	...	HCN, HNC
	IRAS22198+6336	22:21:27.6	+63:51:42	107.30	5.64	1.3	...	HCN, HNC
	IRAS23033+5951	23:05:25.7	+60:08:08	110.09	-0.07	3.5	...	HCN, HNC
	IRAS23140+6121	23:16:11.7	+61:37:45	111.87	0.82	6.44	...	HCN
UCHII	IRAS02232+6138	02:27:01.0	+61:52:14	133.94	1.06	3.0	...	HCN, HNC
	IRAS02575+6017	03:01:32.3	+60:29:12	138.30	1.56	3.8	...	HCN, HNC
	IRAS03035+5819	03:07:25.6	+58:30:52	139.91	0.20	4.2	...	HCN
	IRAS05393-0156	05:41:49.5	-01:55:17	206.56	-16.34	0.5	...	HNC
	IRAS06053-0622	06:07:46.6	-06:22:59	213.70	-12.60	10.8	...	HCN
	IRAS06056+2131	06:08:41.0	+21:31:01	189.03	0.78	0.8	...	HCN, HNC
	IRAS06058+2138	06:08:54.1	+21:38:25	188.95	0.89	2.2	...	HCN, HNC

Table 2—Continued

Classification	Source name	R.A.	Decl.	l	b	D_{far}	D_{near}	inflow tracer
		J(2000.0)	J(2000.0)	($^{\circ}$)	($^{\circ}$)	(kpc)	(kpc)	
	IRAS06061+2151	06:09:07.8	+21:50:39	188.80	1.03	4.1	...	HCN
	IRAS06084-0611	06:10:51.0	-06:11:54	213.88	-11.84	1.0	...	HCN, HNC
	IRAS06099+1800	06:12:53.3	+17:59:22	192.60	-0.05	2.5	...	HCN, HNC
	IRAS17574-2403	18:00:30.4	-24:04:00	5.89	-0.39	2.0	...	HNC
	IRAS17599-2148	18:03:00.4	-21:48:05	8.14	0.23	4.2	...	HCN, HNC
	IRAS18032-2137	18:06:19.0	-21:37:32	8.67	-0.36	4.8	...	HNC
	IRAS18075-1956	18:10:23.5	-19:56:15	10.61	-0.37	4.8	...	HCN, HNC
	IRAS18100-1854	18:14:01.1	-18:53:24	11.94	-0.62	5.2	...	HNC
	IRAS18162-2048	18:19:11.9	-20:47:34	10.84	-2.59	1.9	...	HCN, HNC
	IRAS18174-1612	18:20:24.8	-16:11:35	15.03	-0.68	2.1	...	HCN
	IRAS18317-0757	18:34:24.9	-07:54:48	23.95	0.15	6.0	...	HCN
	IRAS18403-0417	18:42:58.2	-04:14:00	28.20	-0.05	9.1	...	HNC
	IRAS18434-0242	18:46:03.9	-02:39:22	29.96	-0.03	7.4	...	HCN,HNC
	IRAS18469-0132	18:49:34.7	-01:29:08	31.40	-0.26	7.3	...	HCN
	IRAS19095+0930	19:11:53.3	+09:35:46	43.79	-0.13	9.0	...	HNC
	IRAS20081+3122	20:10:09.1	+31:31:34	69.54	-0.98	3.0	...	HNC
	IRAS20255+3712	20:27:26.6	+37:22:48	76.38	-0.62	1.0	...	HCN, HNC
	IRAS20178+4046	20:19:39.3	+40:56:30	78.44	2.66	3.3	...	HCN, HNC
	IRAS20350+4126	20:36:52.6	+41:36:32	80.87	0.42	2.1	...	HCN, HNC
	IRAS22176+6303	22:19:18.2	+63:18:46	106.80	5.31	0.9	...	HCN, HNC
	IRAS22543+6145	22:56:19.1	+62:01:57	109.87	2.12	0.7	...	HCN, HNC
	IRAS23133+6050	23:15:31.5	+61:07:09	111.61	0.37	5.2	...	HCN
	IRAS23138+5945	23:16:04.8	+60:02:00	111.28	-0.66	2.5	...	HCN, HNC

Note. — Kinetic distances are quoted from Simon et al. (2006b) (IRDCs), Beuther et al. (2002), Molinari et al. (1996) (HMPOs), and Thompson et al. (2006) and references therein (UCHIIs). If the distance ambiguity is resolved, only far and no near distance is noted.

Table 3. Derived HCN line parameters

Classification	Source name	v_{thick} (km s ⁻¹)	v_{thin} (km s ⁻¹)	Δv_{thin} (km s ⁻¹)	δv	Profile(δv)
qIRDCc	G028.37_MM9	78.37 (0.041)	79.69 (0.217)	3.25 (0.509)	-0.41 (0.102)	Blue
	G035.39_MM5	43.83 (0.054)	45.01 (0.156)	2.30 (0.377)	-0.51 (0.124)	Blue
aIRDCc	G022.35_MM1 ^a	44.85 (0.190)	44.55 (0.162)	2.97 (0.404)	0.10 (0.119)	Neutral
	G030.97_MM1	78.30 (0.035)	77.85 (0.068)	1.91 (0.146)	0.24 (0.057)	Neutral
	G031.97_MM1	93.92 (0.211)	94.63 (0.079)	3.81 (0.272)	-0.19 (0.077)	Neutral
	G033.69_MM4	104.46 (0.103)	106.00 (0.240)	3.66 (0.644)	-0.42 (0.120)	Blue
	G033.69_MM5	105.49 (0.087)	105.13 (0.106)	1.57 (0.324)	0.23 (0.132)	Neutral
	G034.43_MM4	54.86 (0.057)	57.47 (0.066)	3.46 (0.194)	-0.76 (0.055)	Blue
	G035.39_MM7	45.02 (0.109)	45.56 (0.150)	1.83 (0.315)	-0.29 (0.150)	Blue
	G048.65_MM1	33.82 (0.046)	34.22 (0.076)	0.87 (0.161)	-0.46 (0.165)	Blue
	G053.25_MM4	24.57 (0.030)	24.12 (0.097)	1.09 (0.202)	0.41 (0.139)	Red
	G053.25_MM6	23.45 (0.042)	23.31 (0.119)	1.26 (0.209)	0.11 (0.129)	Neutral
HMPO	IRAS00117+6412	-35.97 (0.079)	-36.03 (0.111)	0.92 (0.412)	0.06 (0.209)	Neutral
	IRAS05358+3543	-17.84 (0.025)	-17.31 (0.070)	1.95 (0.183)	-0.28 (0.055)	Blue
	IRAS05373+2349	2.09 (0.030)	2.29 (0.083)	1.56 (0.288)	-0.13 (0.076)	Neutral
	IRAS18151-1208	33.02 (0.014)	33.61 (0.100)	2.20 (0.236)	-0.27 (0.059)	Blue
	IRAS18182-1433	58.30 (0.211)	59.28 (0.116)	3.38 (0.270)	-0.29 (0.099)	Blue
	IRAS18223-1243	44.67 (0.021)	45.29 (0.079)	1.40 (0.217)	-0.44 (0.099)	Blue
	IRAS18264-1152	43.28 (0.034)	43.75 (0.054)	2.63 (0.158)	-0.18 (0.035)	Neutral
	IRAS18308-0841	77.72 (0.050)	76.81 (0.128)	2.87 (0.332)	0.32 (0.072)	Red
	IRAS18440-0148	97.53 (0.066)	98.03 (0.160)	2.29 (0.259)	-0.22 (0.102)	Neutral
	IRAS18445-0222	86.96 (0.045)	86.94 (0.259)	2.46 (0.672)	0.01 (0.123)	Neutral
	IRAS18447-0229	102.43 (0.133)	102.43 (0.134)	1.37 (0.291)	-0.00 (0.194)	Neutral
	IRAS18470-0044	97.27 (0.100)	96.30 (0.135)	2.99 (0.379)	0.32 (0.089)	Red
	IRAS18527+0301	74.94 (0.075)	75.75 (0.179)	2.42 (0.465)	-0.33 (0.123)	Blue
	IRAS18530+0215	77.07 (0.022)	77.08 (0.087)	2.78 (0.233)	-0.01 (0.039)	Neutral
	IRAS19012+0536	64.84 (0.111)	65.58 (0.151)	2.08 (0.385)	-0.36 (0.142)	Blue
	IRAS19035+0641	32.41 (0.078)	32.33 (0.184)	2.64 (0.502)	0.03 (0.099)	Neutral
	IRAS19410+2336	22.13 (0.016)	22.70 (0.116)	2.66 (0.287)	-0.22 (0.055)	Neutral
	IRAS19411+2306	29.31 (0.026)	29.34 (0.109)	1.62 (0.248)	-0.02 (0.084)	Neutral
	IRAS19413+2332	20.03 (0.024)	20.29 (0.132)	1.47 (0.256)	-0.18 (0.111)	Neutral
	IRAS20126+4104	-3.80 (0.025)	-3.65 (0.070)	2.55 (0.194)	-0.06 (0.037)	Neutral
	IRAS20216+4107	-1.65 (0.032)	-1.59 (0.094)	1.03 (0.218)	-0.07 (0.123)	Neutral
	IRAS20343+4129	11.48 (0.016)	11.48 (0.109)	2.38 (0.230)	0.00 (0.052)	Neutral
	IRAS22134+5834	-17.82 (0.076)	-18.39 (0.106)	1.69 (0.337)	0.33 (0.127)	Red
	IRAS22198+6336	-11.24 (0.029)	-11.05 (0.083)	1.32 (0.238)	-0.15 (0.089)	Neutral
	IRAS23033+5951	-53.18 (0.033)	-53.28 (0.143)	2.52 (0.318)	0.04 (0.070)	Neutral
	IRAS23140+6121	-53.18 (0.033)	-50.74 (0.244)	1.43 (0.496)	-1.71 (0.626)	Blue
	UCHII	IRAS02232+6138	-47.78 (0.024)	-46.55 (0.035)	3.43 (0.092)	-0.36 (0.020)
IRAS02575+6017		-38.13 (0.018)	-37.94 (0.060)	2.35 (0.150)	-0.08 (0.034)	Neutral
IRAS03035+5819		-39.60 (0.024)	-39.57 (0.061)	1.69 (0.160)	-0.02 (0.050)	Neutral
IRAS06053-0622		9.53 (0.029)	10.07 (0.084)	1.29 (0.204)	-0.42 (0.110)	Blue
IRAS06056+2131		2.55 (0.007)	2.74 (0.057)	2.28 (0.137)	-0.08 (0.029)	Neutral
IRAS06058+2138		3.36 (0.008)	3.35 (0.053)	2.69 (0.126)	0.01 (0.023)	Neutral
IRAS06061+2151		-1.26 (0.015)	-0.30 (0.084)	2.58 (0.203)	-0.37 (0.048)	Blue

Table 3—Continued

Classification	Source name	v_{thick} (km s ⁻¹)	v_{thin} (km s ⁻¹)	Δv_{thin} (km s ⁻¹)	δv	Profile(δv)
	IRAS06084-0611	11.65 (0.014)	11.09 (0.034)	2.88 (0.090)	0.20 (0.018)	Neutral
	IRAS06099+1800	7.33 (0.007)	7.35 (0.031)	2.30 (0.083)	-0.01 (0.017)	Neutral
	IRAS17599-2148	20.24 (0.023)	20.61 (0.265)	6.31 (0.746)	-0.06 (0.046)	Neutral
	IRAS18075-1956	-3.99 (0.113)	-2.95 (0.244)	4.81 (0.627)	-0.22 (0.079)	Neutral
	IRAS18162-2048	11.22 (0.043)	12.40 (0.062)	2.77 (0.154)	-0.43 (0.045)	Blue
	IRAS18174-1612	19.66 (0.014)	19.45 (0.059)	3.09 (0.162)	0.07 (0.024)	Neutral
	IRAS18317-0757	78.41 (0.050)	79.86 (0.067)	2.91 (0.167)	-0.50 (0.049)	Blue
	IRAS18434-0242	96.52 (0.027)	97.38 (0.051)	3.66 (0.137)	-0.23 (0.023)	Neutral
	IRAS18469-0132	87.37 (0.024)	88.09 (0.187)	3.04 (0.474)	-0.24 (0.079)	Neutral
	IRAS20255+3712	-1.52 (0.020)	-1.37 (0.084)	2.09 (0.255)	-0.07 (0.051)	Neutral
	IRAS20178+4046	1.03 (0.016)	1.03 (0.071)	1.64 (0.152)	0.00 (0.053)	Neutral
	IRAS20350+4126	-3.88 (0.035)	-2.85 (0.089)	2.33 (0.229)	-0.44 (0.069)	Blue
	IRAS22176+6303	-6.80 (0.007)	-6.77 (0.030)	2.63 (0.071)	-0.01 (0.014)	Neutral
	IRAS22543+6145	-12.41 (0.018)	-10.40 (0.056)	3.01 (0.144)	-0.67 (0.040)	Blue
	IRAS23133+6050	-56.48 (0.020)	-56.16 (0.055)	2.49 (0.148)	-0.13 (0.031)	Neutral
	IRAS23138+5945	-44.56 (0.055)	-44.64 (0.145)	3.33 (0.339)	0.02 (0.060)	Neutral

Note. — ^a – The $F=0-1$ hyperfine component is adopted as a standard for δv calculation.

Table 4. Derived HNC line parameters

Classification	Source name	v_{thick} (km s ⁻¹)	v_{thin} (km s ⁻¹)	Δv_{thin} (km s ⁻¹)	δv	Profile(δv)	$\frac{T(B)}{T(R)}$	Profile($\frac{T(B)}{T(R)}$)	v_{dip} (km s ⁻¹)
qIRDCc	G028.37_MM9	78.48 (0.028)	80.16 (0.062)	2.63 (0.144)	-0.64 (0.049)	Blue	5.66	Blue	80.82
	G031.97_MM9	96.06 (0.051)	96.75 (0.202)	5.39 (0.456)	-0.13 (0.048)	Neutral	1.21	Neutral	97.27
	G035.39_MM5	44.12 (0.029)	45.51 (0.059)	1.64 (0.165)	-0.85 (0.101)	Blue
aIRDCc	G015.31_MM3	31.27 (0.105)	31.04 (0.057)	0.99 (0.116)	0.23 (0.166)	Neutral
	G023.60_MM1	106.75 (0.044)	106.74 (0.137)	4.35 (0.319)	0.00 (0.042)	Neutral	0.94	Neutral	106.25
	G023.60_MM6	53.10 (0.040)	53.23 (0.081)	1.77 (0.182)	-0.08 (0.069)	Neutral
	G024.60_MM1	54.11 (0.035)	53.11 (0.091)	1.88 (0.196)	0.53 (0.087)	Red
	G028.37_MM4	78.50 (0.023)	79.31 (0.066)	3.17 (0.157)	-0.41 (0.035)	Blue
	G028.37_MM6	78.32 (0.054)	80.29 (0.043)	2.37 (0.105)	-0.83 (0.055)	Blue	3.26	Blue	81.44
	G030.97_MM1	77.95 (0.018)	77.95 (0.075)	2.47 (0.197)	-0.00 (0.038)	Neutral
	G031.97_MM1	94.34 (0.026)	95.42 (0.058)	3.51 (0.140)	-0.31 (0.027)	Blue
	G031.97_MM8	94.25 (0.065)	94.70 (0.079)	2.46 (0.245)	-0.18 (0.061)	Neutral	2.62	Blue	97.89
	G033.69_MM4	105.78 (0.048)	106.11 (0.071)	3.35 (0.180)	-0.10 (0.036)	Neutral
	G033.69_MM5	105.20 (0.035)	105.25 (0.073)	1.97 (0.193)	-0.02 (0.055)	Neutral
	G034.43_MM1	58.14 (0.024)	57.79 (0.052)	2.85 (0.116)	0.12 (0.027)	Neutral	0.56	Red	57.26
	G034.43_MM3	59.48 (0.029)	59.41 (0.039)	2.15 (0.103)	0.03 (0.032)	Neutral
	G034.43_MM4	56.75 (0.035)	57.76 (0.039)	2.47 (0.098)	-0.41 (0.034)	Blue
	G035.59_MM3	44.40 (0.036)	44.76 (0.065)	1.34 (0.137)	-0.27 (0.080)	Blue
	G038.95_MM3	42.58 (0.040)	42.27 (0.094)	2.20 (0.249)	0.14 (0.063)	Neutral
	G038.95_MM4	42.03 (0.040)	42.30 (0.107)	1.40 (0.307)	-0.19 (0.113)	Neutral
	G048.65_MM1	33.78 (0.030)	34.03 (0.120)	1.65 (0.257)	-0.15 (0.094)	Neutral
	G048.65_MM2	33.62 (0.032)	33.85 (0.106)	1.07 (0.209)	-0.22 (0.136)	Neutral
	G053.25_MM4	24.48 (0.012)	24.43 (0.040)	1.19 (0.094)	0.04 (0.044)	Neutral
G053.25_MM6	23.55 (0.019)	23.74 (0.089)	1.45 (0.178)	-0.13 (0.077)	Neutral	
G053.31_MM2	25.03 (0.029)	25.57 (0.086)	1.31 (0.216)	-0.41 (0.111)	Blue	
HMPO	IRAS05358+3543	-17.64 (0.013)	-17.40 (0.076)	1.74 (0.201)	-0.14 (0.054)	Neutral
	IRAS05373+2349	2.26 (0.016)	2.42 (0.072)	1.57 (0.218)	-0.10 (0.058)	Neutral
	IRAS18024-2119	0.93 (0.117)	0.60 (0.063)	2.11 (0.153)	0.15 (0.086)	Neutral
	IRAS18089-1732	34.34 (0.069)	32.78 (0.080)	3.39 (0.170)	0.46 (0.050)	Red	0.47	Red	33.36
	IRAS18102-1800	21.67 (0.058)	21.41 (0.086)	2.07 (0.196)	0.13 (0.071)	Neutral
	IRAS18144-1723	47.86 (0.040)	47.61 (0.076)	3.29 (0.180)	0.08 (0.035)	Neutral	0.77	Red	47.78
	IRAS18151-1208	33.10 (0.020)	33.37 (0.073)	1.89 (0.180)	-0.14 (0.051)	Neutral
	IRAS18162-1612	61.86 (0.028)	61.86 (0.092)	1.77 (0.228)	-0.00 (0.068)	Neutral
	IRAS18182-1433	58.85 (0.031)	59.66 (0.112)	3.04 (0.258)	-0.26 (0.052)	Blue
	IRAS18223-1243	45.33 (0.025)	45.29 (0.067)	1.85 (0.156)	0.03 (0.050)	Neutral
	IRAS18264-1152	43.99 (0.017)	43.83 (0.076)	2.41 (0.183)	0.07 (0.039)	Neutral
	IRAS18290-0924	84.29 (0.064)	84.47 (0.111)	1.98 (0.267)	-0.09 (0.089)	Neutral
	IRAS18310-0825	84.46 (0.076)	84.67 (0.089)	1.83 (0.222)	-0.12 (0.091)	Neutral
	IRAS18345-0641	95.46 (0.082)	95.48 (0.063)	1.79 (0.152)	-0.01 (0.081)	Neutral
	IRAS18440-0148	97.69 (0.029)	97.67 (0.153)	1.47 (0.433)	0.02 (0.124)	Neutral
	IRAS18470-0044	96.49 (0.067)	96.31 (0.162)	2.52 (0.462)	0.07 (0.092)	Neutral	0.59	Red	95.71
	IRAS18488+0000	82.78 (0.141)	83.36 (0.182)	2.95 (0.439)	-0.20 (0.113)	Neutral
IRAS18511+0146	57.10 (0.038)	56.94 (0.061)	1.77 (0.145)	0.09 (0.056)	Neutral	
IRAS18530+0215	77.25 (0.016)	77.30 (0.100)	2.73 (0.219)	-0.02 (0.042)	Neutral	
IRAS19220+1432	69.27 (0.104)	69.78 (0.298)	3.11 (0.516)	-0.16 (0.132)	Neutral	

Table 4—Continued

Classification	Source name	v_{thick} (km s ⁻¹)	v_{thin} (km s ⁻¹)	Δv_{thin} (km s ⁻¹)	δv	Profile(δv)	$\frac{T(B)}{T(R)}$	Profile($\frac{T(B)}{T(R)}$)	v_{dip} (km s ⁻¹)
	IRAS19411+2306	29.35 (0.019)	29.24 (0.088)	1.60 (0.233)	0.12 (0.110)	Neutral
	IRAS20126+4104	-3.45 (0.015)	-3.95 (0.048)	1.95 (0.110)	0.26 (0.035)	Red
	IRAS20216+4107	-1.57 (0.025)	-1.63 (0.054)	0.97 (0.118)	0.06 (0.082)	Neutral
	IRAS20293+3952	6.06 (0.026)	5.96 (0.117)	2.32 (0.281)	0.04 (0.062)	Neutral
	IRAS20343+4129	11.15 (0.022)	11.73 (0.123)	2.29 (0.261)	-0.25 (0.070)	Blue
	IRAS22134+5834	-18.24 (0.064)	-18.80 (0.142)	1.54 (0.260)	0.37 (0.147)	Red	0.94	Neutral	-18.40
	IRAS22198+6336	-11.12 (0.061)	-10.97 (0.065)	1.25 (0.164)	-0.12 (0.102)	Neutral
	IRAS23033+5951	-52.79 (0.034)	-53.69 (0.185)	3.13 (0.450)	0.29 (0.081)	Red
UCHII	IRAS02232+6138	-46.88 (0.033)	-46.35 (0.077)	2.90 (0.178)	-0.18 (0.040)	Neutral
	IRAS02575+6017	-38.24 (0.019)	-37.97 (0.067)	1.37 (0.145)	-0.20 (0.066)	Neutral
	IRAS05393-0156	10.34 (0.046)	9.47 (0.074)	0.57 (0.148)	1.52 (0.447)	Red	1.09	Neutral	10.57
	IRAS06056+2131	2.67 (0.010)	2.83 (0.107)	2.58 (0.277)	-0.06 (0.046)	Neutral
	IRAS06058+2138	3.31 (0.010)	3.40 (0.075)	2.00 (0.182)	-0.04 (0.043)	Neutral
	IRAS06084-0611	11.69 (0.020)	11.31 (0.077)	2.25 (0.185)	0.17 (0.045)	Neutral
	IRAS06099+1800	7.32 (0.010)	7.32 (0.082)	1.79 (0.205)	-0.00 (0.052)	Neutral
	IRAS17574-2403	9.01 (0.017)	8.95 (0.032)	3.78 (0.087)	0.02 (0.013)	Neutral
	IRAS17599-2148	20.10 (0.031)	18.87 (0.106)	4.15 (0.241)	0.30 (0.037)	Red	0.38	Red	18.00
	IRAS18032-2137	33.50 (0.047)	35.10 (0.041)	4.48 (0.110)	-0.36 (0.021)	Blue	3.32	Blue	37.74
	IRAS18075-1956	-3.13 (0.029)	-2.00 (0.193)	2.75 (0.472)	-0.41 (0.107)	Blue
	IRAS18162-2048	12.36 (0.024)	12.46 (0.130)	2.37 (0.262)	-0.04 (0.065)	Neutral	1.30	Blue	12.51
	IRAS18100-1854	39.96 (0.037)	38.37 (0.051)	3.95 (0.112)	0.40 (0.025)	Red	0.41	Red	36.99
	IRAS18403-0417	96.26 (0.053)	95.74 (0.071)	4.44 (0.186)	0.12 (0.028)	Neutral	1.62	Blue	97.56
	IRAS18434-0242	96.85 (0.015)	97.56 (0.055)	3.02 (0.137)	-0.24 (0.026)	Neutral
	IRAS19095+0930	44.12 (0.062)	44.12 (0.247)	4.77 (0.610)	0.00 (0.065)	Neutral
	IRAS20081+3122	12.52 (0.022)	11.74 (0.068)	3.91 (0.168)	0.20 (0.025)	Neutral
	IRAS20255+3712	-1.41 (0.019)	-1.49 (0.074)	1.92 (0.215)	0.04 (0.049)	Neutral
	IRAS20178+4046	0.98 (0.012)	1.07 (0.097)	1.87 (0.216)	-0.05 (0.058)	Neutral
	IRAS20350+4126	-3.01 (0.035)	-2.46 (0.110)	2.27 (0.282)	-0.24 (0.071)	Neutral
	IRAS22176+6303	-6.84 (0.008)	-6.83 (0.082)	2.27 (0.184)	-0.01 (0.040)	Neutral
	IRAS22543+6145	-11.38 (0.024)	-10.61 (0.117)	2.80 (0.268)	-0.27 (0.057)	Blue	1.78	Blue	-10.12
	IRAS23138+5945	-44.49 (0.031)	-44.44 (0.155)	2.12 (0.381)	-0.03 (0.088)	Neutral

Table 5. Blue excess (E) statistics

Evolutionary stage	Inflow Tracer	N_{Blue}	N_{Red}	N_{Total}	E	P
IRDCs	HCN	6	1	12	0.42	0.062
	HNC	8	1	25	0.28	0.019
HMPOs	HCN	7	3	26	0.15	0.172
	HNC	2	4	28	-0.07	0.891
UCHIIs	HCN	7	0	23	0.30	0.008
	HNC	3	3	23	0.00	0.500